Magnetic Nanoparticle Aggregation and Complete De-Encapsulation of Such Aggregates from a Liquid Drop Interior

Swarup Kumar Subudhi, Ghansham Rajendrasingh Chandel, Vishal Sankar Sivasankar, and Siddhartha Das*

Department of Mechanical Engineering, University of Maryland, College Park, MD 20742

*Email: sidd@umd.edu

Abstract

Magnetic nanoparticles (MNPs) have been extensively used for drug delivery, on-demand material deposition, etc. In this study, we demonstrate the capability to extract MNPs on-demand from a magnetic nanoparticle laden drop (MNLD) (i.e., a drop of stable aqueous dispersion of MNPs) suspended inside a highly viscous polymer (PDMS) medium in the presence of an external applied magnetic field. The phenomena involve the aggregation of MNPs inside the drop and the consequent extraction of the MNPs out of the drop with the drop retaining its original shape post-extraction. We define this latter phenomenon as de-encapsulation. This is the first study, which to the best of our knowledge, demonstrates such a removal of NPs from the interior of a drop (where the NPs, which were originally inside the drop, breach the drop interface, and get completely separated from the drop) without any permanent deformation of the drop. We further discuss how the changes in the MNP concentration and the drop volume affect the de-encapsulation distance (i.e., the distance between the drop and the location of the magnet, at the time instant when the particles leave the drop) and identify the volume of the aggregates extracted from the drop along with the mechanisms causing such de-encapsulation. We propose a theory to describe the process; our theoretical predictions capture the experimental trends well. Overall, our results in addition to demonstrating the first-of-its-kind de-encapsulation of NPs from drop interior, demonstrate a method to control the dynamics, extraction, and targeted deposition of MNPs.

2

Introduction

The dynamics of nanoparticle (NP) or microparticle laden liquid drops have been probed extensively [1-7] owing to its significance in applications such as droplet-based printing (such as inkjet printing or aerosol jet printing) of conductive and colloidal inks [8-13] as well as understanding the formation and dynamics of aerosol [14] and contamination by particulate matter [15,16]. At the same time, such nanoparticle-laden liquid drops have been known to provide excellent platforms for manipulating these nanoparticles (NPs) by making them undergo processes such as aggregation inside the drop [17-19], aggregation during drop evaporation (such aggregation can lead to uniform deposits or "coffee-stain"-like non-uniform deposits) [20-22], and adsorption and self-assembly at the drop-fluid interface [23,24]. Triggering interactions between NPs at the interface of a liquid drop is often facilitated by large capillary forces that these NPs experience at the interface. In fact, a generic fluid-fluid interface (not necessarily belonging to a liquid drop) utilizes the large capillary forces, imparted to the NPs by the air-water or water-oil interface, to often manipulate the ordering and self-assembly of those particles at the interface [25-27]. This same large capillary force imparted by the interface hinders the extraction of NPs originally present within a liquid drop, and thus, offers a stable interface environment for ordering and self-assembling NPs. However, the controlled aggregation and extraction of the NPs (or functionalized NPs) can be utilized as a system for targeted drug delivery [28-32], etc. Such extraction of NPs in the presence of an applied force field (electrical, magnetic, etc.) from a NP-laden drop, which we term as de-encapsulation in this study and refers to the NPs breaching the drop-fluid interface and coming out of the drop *completely* (i.e., *complete de-encapsulation*) with the drop shape remaining intact at the end of the process, has rarely been demonstrated in the existing literature.

3

Magnetic nanoparticles (MNPs), such as Fe_3O_4 are known to be biocompatible and have been extensively studied in the context of drug-delivery [28-32] and magnetic-field induced self-assembly and ordering [33-37] in various fluid media. The behavior of the MNPs dispersed in a fluid medium under an applied magnetic field provides insights into the kinetics and structured ordering of the MNPs [38,39] in the bulk and at the fluid interface. However, there is very scarce evidence of the *de-encapsulation* phenomenon of these magnetic NPs from a magnetic nanoparticle laden drop (MNLD) suspended in an immiscible fluid medium. In fact, to the best of our knowledge, there is little evidence of any type of NPs (or NP aggregate) undergoing controlled *de-encapsulation* from the interior of a liquid drop, given the fact that such de-encapsulation will entail the particles (from the interior of the drop) coming out of the drop entirely by breaching the very strong capillary forces at the drop-fluid interface. Achieving such *de-encapsulation* will be a major breakthrough since this will imply that we can achieve *on-demand* particle deposition at desired locations by simply transporting the particle-laden liquid drop to such locations and triggering the de-encapsulation.

In this study, we achieve this remarkable feat: we are able to enforce *controlled and complete de-encapsulation* of magnetic nanoparticles (in the form of nanoaggregates) from the interior of a MNLD. Specifically, we achieve the *de-encapsulation* of the polyvinylpyrrolidone(PVP)-coated Fe_3O_4 NPs. We start with such PVP-coated Fe_3O_4 NPs dispersed in an aqueous drop that is inserted into a partially uncured polymer medium, i.e., polydimethylsiloxane (PDMS). On subjecting the MNLD to a non-linear strong magnetic field (i.e. max magnetic field strength of ~0.2 mT), we observe that (1) the drop moves in the direction of increasing magnetic field, (2) aggregation of MNPs occur within the drop at the drop-PDMS interface (in the direction of the applied magnetic field) leading to a sub-millimetric sized

4

aggregate, (3) subsequent *complete de-encapsulation* of this aggregate from the interior of the drop, and (4) the drop returning back to its previous spherical shape. The de-encapsulation is characterized by (1) the distance from the magnet at which the de-encapsulation of the aggregate occurs (this distance is denoted as the de-encapsulation distance, or h_{de}) and (2) the volume of the de-encapsulated aggregate (V_{agg}). We characterize the de-encapsulation phenomenon by quantifying h_{de} and V_{agg} as functions of the drop volume (V_d) and the concentration of the magnetic NPs (c_{MNP}) inside the drop. The underlying key to this phenomenon is ensuring that the aggregate (inside the drop) is subjected to the magnetic field (that varies inversely as h_{de}) that ensures a magnetic force (that scales V_{agg}) that is large enough to overcome the resisting water-PDMS capillary force (that scale as the length of the aggregate). We develop a theoretical model that accounts for these physical factors and the resulting theoretical prediction matches well with the experimental trends. We anticipate that this technique of achieving the *complete de-encapsulation of NP aggregates* from the drop interior that has been introduced here will be matured further in near future enabling de-encapsulation of other types of particles in less viscous media (such as air or oil), thereby providing pathways to wide-ranging applications (e.g., 3D printing) that rely on the "on-demand" and controllable particle deposition at desired locations and in desired amounts.

5

Materials and Methods

Materials:

The fluid medium used for the experiments in this study is a 2-hour room temperature (T_{amb} = 25°C) cross-linked PDMS (mixing ratio A:B = 10:1) polymer (δ_{PDMS} = 6.02%, zero-shear viscosity $\eta_{zs} \sim 4.01$ Pa.s, density = 1087 kg/m^3). The PDMS (Sylgard-184) kit was procured from Sigma-Aldrich, and its corresponding curing curve and rheology profile are given in **Figure S1**. The super paramagnetic nanoparticles used in this study are PVP-coated spherical Fe_3O_4 NPs (purity: 99%, average particle size: 20-30nm) procured from US Research Nanomaterials Inc., and its corresponding magnetization curve is shown in **Figure S2**. The NdFeB permanent bar magnets used in this study are of the N35 grade. The magnets were stacked to achieve the required magnetic field strength that was suitable for observing the phenomenon in the given setup, and the field contours in the experimental domain as measured using a portable magnetometer are as shown in **Figure S3**.

Sample Preparations:

Aqueous dispersions of Poly-vinyl Pyrrolidone (PVP) coated Fe_3O_4 MNPs were prepared corresponding to weight by volume concentrations of 10, 15, 20 mg/ml. The dispersions were mechanically stirred at room temperature (T_{amb} = 25°C) and prepared on an ultrasonication bath (47 kHz, continuous mode) for 1 hour.

6

Imaging and Imaging Corrections:

A hi-speed camera FASTCAM Photron was used to capture the phenomenon from the X-Z viewing plane. A continuous high-luminosity light source was used to make image capturing better at higher frame rates. In the Y-Z viewing plane, a secondary camera (Nikon D5300, NIKKOR 18-55mm lens) was used to capture image data in the orthogonal plane which was further used for estimating the volume of the aggregate using the images captured from both viewing planes. Scaling and Refractive corrections were applied on the images and videos captured from the cameras based on change in dimensions and warpage of a planar grid placed inside PDMS medium as compared to that in air at a fixed focal length for both cameras. The corrected images and videos were used for data extraction.

De-encapsulation Length Calculation:

The images at the time of de-encapsulation were extracted from the videos and the de-encapsulation distance was measured in pixels from the images using Adobe Photoshop, and subsequently pixel-to-mm scaling was done to calculate the values.

Aggregate Volume Data Extraction:

After the images from the cameras of the two orthogonal viewing planes were captured and required refractive corrections were done, both the images were brought to the same scale and the corresponding scaling factors were recorded for pixel to mm conversion. A MATLAB code was used to measure the volume of the aggregate extracted from the 2D images, by suitable fitting methods assuming the aggregate to be axisymmetric and ellipsoidal in cross-section as shown in **Figure S4**.

RESULTS

Nanoparticle aggregation and de-encapsulation

Figure 1 describes the experimental set up and the two main findings of the paper. The experimental set up consists of a magnetic (PVP coated Fe_3O_4) NP-laden drop being introduced inside an uncured (or partially cured) PDMS bath. There are two cameras positioned in the X-Z and Y-Z viewing planes to observe the dynamics of the magnetic NP-laden drop (MNLD). The PDMS bath rests on a fixture over a bar magnet stack, which attracts the magnetic-NP-laden drop towards itself. The partially cured PDMS (i.e., outgassed and left for 2 h after mixing crosslinker) has a higher density than the MNLD, and hence in the absence of the magnetic field, the drop will tend to move vertically up inside the PDMS bath. Also, such smaller density of the MNLD implies that if the drop is released at a distance greater than a critical value (i.e., h_{cr}) from the top surface of the magnet, the magnetic force on the drop, which decreases non-linearly with an increase in the distance between the drop and the bar magnet, is smaller than the buoyant force on the drop enforcing the drop to move away from the magnet (see **Figure 2**). Here we consider that the drop is released at a distance (from the magnet) lesser than h_{cr} and this causes the magnetic-field-driven attraction of the MNLD towards the magnet, thereby leading to two distinct effects, namely the NP aggregation inside the drop and the *de-encapsulation* of such aggregates from the interior of the drop in a manner such that the entire nanoaggregate leaves the drop without the drop getting permanently deformed. Below, we describe these two effects in detail.

First, we find that the NPs *aggregate inside the drop and localize inside the drop at locations that are closest to the magnet.* This progressive aggregation can be noted from the constant brightening of the locations in the interior of the drop from where the NPs move away to form the nanoaggregates. A darker color of the drop interior suggests that there is the presence of the NPs;

8

however, when the color of the drop interior at such locations becomes brighter, it indicates that a scarce number of NPs are present at such locations [see **Figure 1(b)**]. We also consider such aggregation of MNPs inside the MNLD and the subsequent nanoaggregate de-encapsulation for the MNLD created using a stronger aqueous dispersion of Fe_3O_4 [see **Figure 1(c)**]. For this case, one observes a faster aggregation and de-encapsulation (as can be noted from the corresponding timestamps).

This aggregated mass of the NPs accumulates at the drop-PDMS interface at the location that is closest to the magnetic field. Subsequently, the presence of the magnetic field pulls the magnetic nanoaggregate downward and eventually the nanoaggregate gets completely extracted out of the drop with the drop itself retaining its spherical shape after the extraction [see **Figure 1 (b)** and video **M1**]. Such pulling out of the MNPs or (MNP aggregates) from inside the drop in a manner such that the nanoaggregate gets completely detached from the drop and the drop remains intact, represents a most unique and remarkable situation where *there is an almost complete de-encapsulation of the aggregated particles from the interior of a drop*. Very often particles localize at the drop-air or drop-liquid interface [40-41], but never completely de-encapsulates from the drop, typically stemming from the very large capillary forces that these particles must overcome for completely breaching the interface. In the present case, however, a large magnetic force acts on the nanoaggregates – this high magnetic force stems from a combination of the MNPs forming an aggregate, i.e., creating a highly concentrated zone of the MNPs, and the presence of a strong magnetic field – and enables the aggregate to overcome the restraining capillary force exerted by the drop-PDMS interface. To the best of our knowledge, this is the first study that shows such de-encapsulation of particles from the interior of a liquid drop.
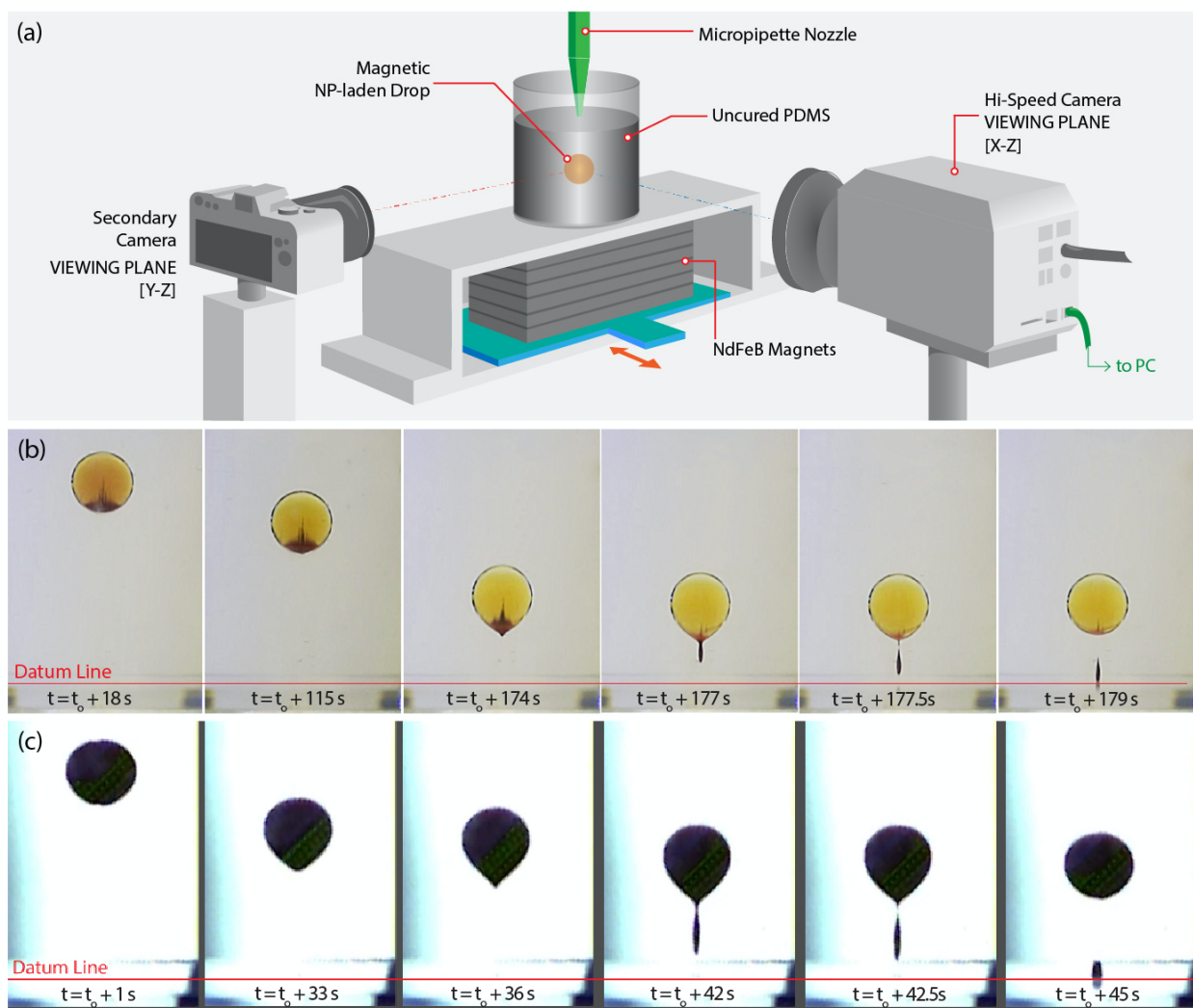
Figure 1. (a) Schematic representation of the Experimental Setup. **(b,c)** Chronological snapshots illustrating the observed phenomena (aggregation of magnetic NPs inside the drop and complete de-encapsulation of the resulting aggregates from the drop interior without any permanent drop deformation) for **(b)** a weak dispersion (with c_{MNP} = 5mg/mL, V_d = 10µL) or a drop containing a weakly dispersed smaller concentration of Fe_3O_4, and **(c)** a strong dispersion (with c_{MNP} = 15mg/mL, V_d = 20µL) or a drop containing a strongly dispersed larger concentration of Fe_3O_4. For case (b), we do not perform ultrasonication of the dispersion (of magnetic NPs inside the water), which leads to a weaker dispersion; on the other hand, for case (c), we performed the

10

ultrasonication of the dispersion, ensuring a stronger dispersion (of magnetic NPs inside the water). This difference in the nature of the dispersion, therefore, stems from the experimental step (with or without ultrasonication). The aggregation process can be clearly visualized for the drop with a weak dispersion [part (b)], which is not the case for the drop with a strong dispersion [part (c)]. The datum line corresponds to the base of the container.

To understand the correct parameters dictating the de-encapsulation, we first identify a critical height, h_{cr}, shown in **Figure 2(a)**. h_{cr} is defined as the critical distance between the center of mass of a MNLD and the top of the magnet stack, such that the buoyancy force on the drop balances magnetic force acting on the drop. Let us define the drop release height, h_{dr}, as the distance between the MNLD (when released into the fluid medium) and the top of the magnet stack. If the drop is so released that $h_{dr} > h_{cr}$, the buoyancy force on the drop dominates, and the drop moves upward till it reaches the free surface [see **Figure 2(a)**]. If the drop is so released that $h_{dr} < h_{cr}$, the magnetic force dominates, and the drop moves downwards in the direction of increasing magnetic field strength [see **Figure 2(a)**]. This is the domain (i.e., the domain corresponding to $h_{dr} < h_{cr}$) where the parametric study has been conducted. In this experimental domain (i.e., $h_{dr} < h_{cr}$), two separate cases were observed. In the first case, the magnetic field induced aggregates (present inside the drop) ensured that the drop gets pushed downwards to the base, with the drop getting deformed [see **Figure 2(b)**] and eventually ending up wetting the base of the container without losing any of the contents (i.e., without any *de-encapsulation*). In the second case, the aggregates, which are formed by the presence of the magnetic field acting on the NPs present inside the drop, again ensure that the drop is pushed downwards, gets deformed considerably until reaching a critical point. At this critical point, a portion of the nanoparticles (in the form of an aggregate), along with some attached water molecules, get pulled out of the drop. This is the phenomenon of *complete de-encapsulation*, where this nanoaggregate comes out of the drop entirely and loses any contact with the drop. This de-encapsulation occurs at the tip of the deformed drop and the released nanoaggregate settles at the base of the container [as shown in **Figure 2(c-i)**]. The drop after partially losing its contents *via* de-encapsulation might either go downwards or upwards. For example, the drop will go downwards and settle at the same location on the base of the container

12

where the released nanoaggregate has deposited, if the drop, even after the de-encapsulation, contains enough NPs to experience large enough magnetic force that overwhelm the vector sum of buoyancy, viscous drag forces [see **Figure 2(c-iii)**]. On the other hand, if after de-encapsulation, the drop no longer contains sufficient MNPs, the magnetic force on the drop becomes weak enabling the buoyant and viscous forces to drive the upwards and away from the base [see **Figure 2(c-ii)**]. For either of the scenarios, there is no permanent deformation of the drop. Here, we define a quantity called the de-encapsulation distance, h_{de}, which is the distance from the de-encapsulation point to the top of the magnet stack [see **Figure 2 (c), Figure 3(a)**]: the de-encapsulation point can be defined as the spatial coordinate at which the aggregate separates completely from the MNLD.
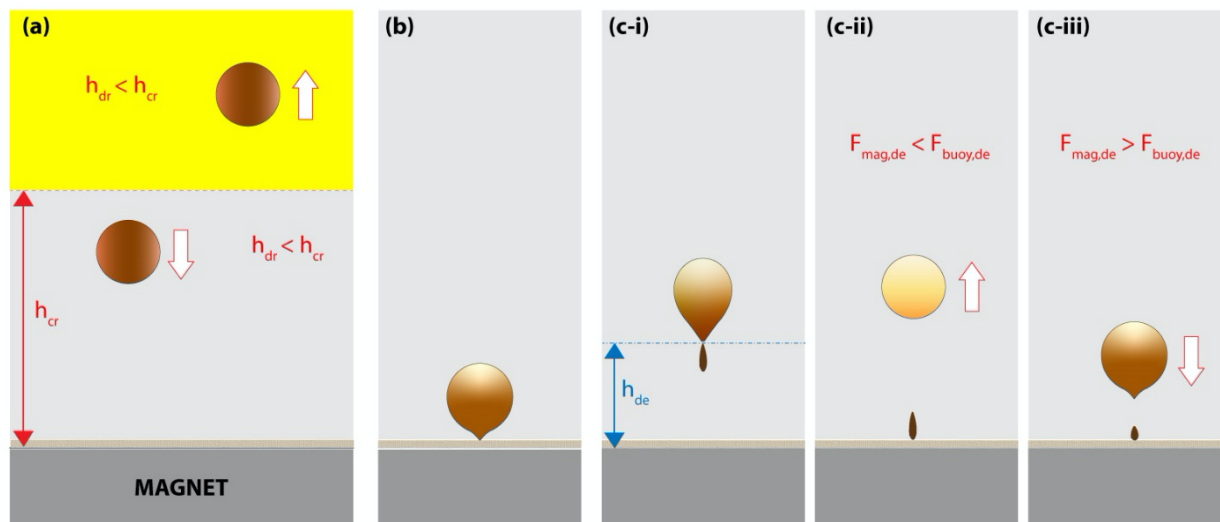
Figure 2. Schematic of different possible outcomes once the drop is released into the fluid medium. **(a)** After the drop has been released, it can either move upwards (if $h_{dr} > h_{cr}$) or move downwards (if $h_{dr} < h_{cr}$). On moving downwards, the NPs first aggregate and then either **(c-i)** the aggregated nanoparticles de-encapsulate from the NP-laden drop at a distance h_{de} or **(b)** the NP-laden reaches the bottom without any de-encapsulation. After de-encapsulation, the drop will either **(c-ii)** move up towards the free surface (this occurs for the case when post de-encapsulation, there is very little amount of MNPs present within the drop) or **(c-iii)** move down and localize on the bottom substrate at locations where the de-encapsulated magnetic nano-aggregate has deposited (this occurs for the case when even after the de-encapsulation, there is a significant amount of MNPs present within the drop).

14

Parametric Analysis of the Particle aggregation and de-encapsulation

For this study, we considered MNLDs with a stable and strong dispersion of Fe_3O_4 NPs [equivalent to the case discussed in Fig. 1(c)], as stated in the Materials and Methods section. Our parametric analysis only considers the effect of varying drop volumes and MNP concentrations inside the drops on the aggregation and de-encapsulation, with all the other variables affecting the process being kept constant in the experiments. Based on trial runs, the drop release distance (h_{dr}) was kept constant at 20mm from the base of the container, the concentration of MNPs (C_{MNP}) was varied between 10 mg/ml to 20 mg/ml, and the drop volumes (V_d) were set at 10, 15, and 20 microliters: these combinations of the C_{MNP} and V_d ensured that the MNLD moved downwards towards the magnetic stack and the dispersions inside the drop can be treated as *strong dispersions*. For this domain of experimental parameters, it was observed that all the MNPs in an MNLD didn't completely aggregate within the time frame of the MNLD reaching the datum line. In addition, the amount of MNPs that aggregated inside the drop prior to de-encapsulation defined the amount of magnetic force acting on the aggregates that drove them to de-encapsulate; this stemmed from the fact that $F_{mag} \propto V_{MNP}$, where V_{MNP} is the volume of MNPs that form an aggregate inside the MNLD.

Specifically, for the case where C_{MNP} = 10 mg/mL and V_d = 10μL, no de-encapsulation was observed. This particular MNLD takes a long time (t_{de} >180s) to reach the datum line and this can be attributed to (1) a low C_{MNP} leading to weak magnetic forces acting on the drop as a whole, (2) a lesser quantity of aggregates formed, and (3) higher capillary forces on the drop-PDMS interface as compared to the magnetic forces acting on the MNPs. However, for all the other cases, de-encapsulation of aggregates was observed.

15

It was observed that both the de-encapsulation distance, h_{de} [shown again in **Figure 3(a)**] and the volume of the de-encapsulated aggregate (V_{agg}) increase with increasing drop volumes (V_d) and the NP concentration (c_{MNP}) within the drop [see **Figures 3(b,c)**]. This implies that the de-encapsulation from a larger drop or from a drop with a greater concentration of the MNPs occurs with the drop being at a greater distance from the magnetic stack and the corresponding size of the de-encapsulated aggregate is also larger. A larger sized drop (with a given c_{MNP}) or a drop (of a given size) with larger C_{MNP} has a greater amount of MNPs. Accordingly, the aggregation starts at a greater distance from the magnetic stack. As a consequence, such aggregates become larger in size quickly and can therefore experience a critical magnetic force, large enough to overcome the resisting buoyancy and the drop-PDMS-interface-induced capillary forces, even at a relatively weaker magnetic field strength (i.e., at a greater distance from the magnetic stack). This explains why both h_{de} and V_{agg} increase with V_d and c_{MNP}. Given that V_{agg} is larger, the drop-PDMS-interface-induced resisting capillary force is also greater (this force scales linearly with the size of the de-encapsulated aggregate). Accordingly, the critical magnetic force on the aggregates that ensures de-encapsulation must also increase with V_d and c_{MNP}. In Figs. 3(d,e), we have schematically represented this highly unique interplay between these different factors determining the eventual de-encapsulation of the aggregate.
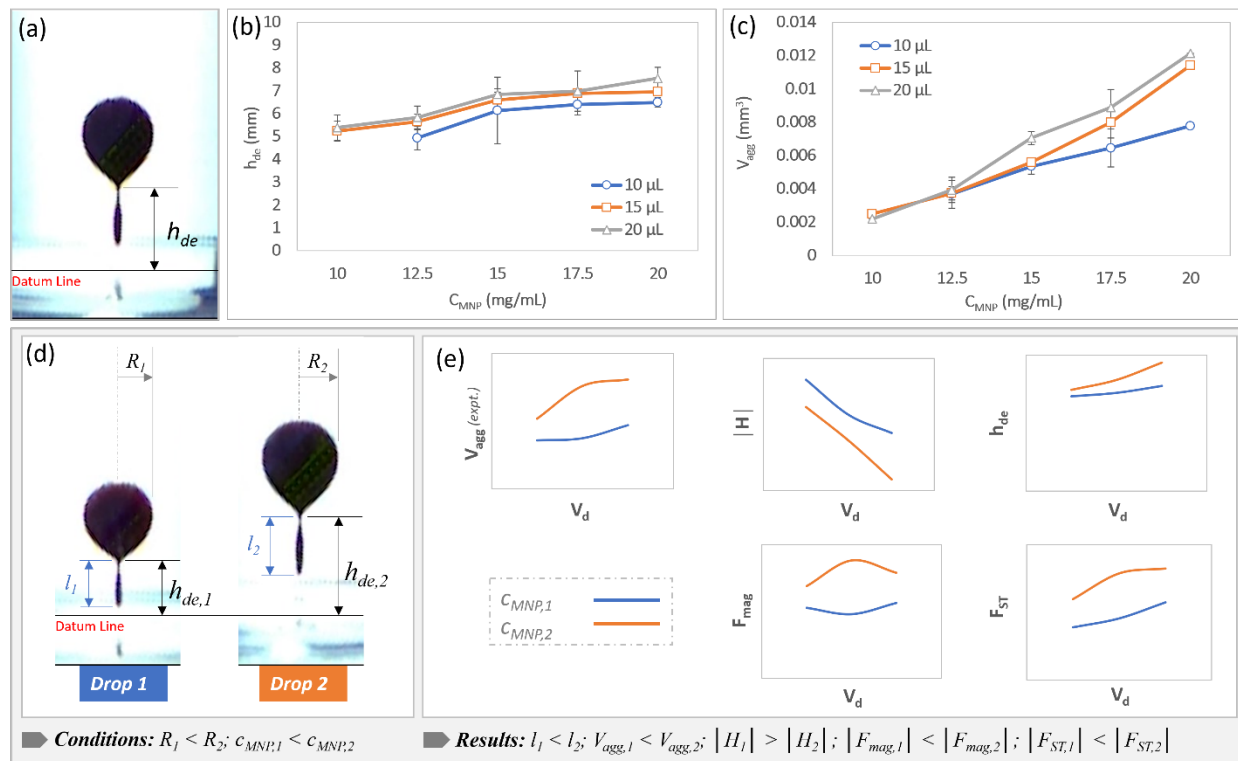
16

Figure 3. (a) Depiction of the de-encapsulation distance (h_{de}). **(b,c)** Variation of **(b)** h_{de} with MNP concentration (C_{MNP}) and **(c)** and the extracted aggregate volume (V_{agg}) with MNP concentration (C_{MNP}). Results have been shown for different values of the drop volume, i.e., V_d = 10, 15 and 20 microliters. **(d)** Schematic of the situation showing the manner in which particle de-encapsulation occurs from two drops of different volumes (V_{d1} and V_{d2}) and different NP concentrations ($c_{MNP,1}$ and $c_{MNP,2}$). The de-encapsulation is characterized by the volumes of the aggregate ($V_{agg,1}$ and $V_{agg,2}$) coming out of the drops, distances ($h_{de,1}$ and $h_{de,2}$) from the substrate at which the de-encapsulation from the two drops occur occurs, and the net magnetic field strengths ($|\mathbf{H}_1|$ and $|\mathbf{H}_2|$), the net driving magnetic forces ($|\mathbf{F}_{mag,1}|$ and $|\mathbf{F}_{mag,2}|$), and the net resisting capillary forces ($|\mathbf{F}_{cap,1}|$ and $|\mathbf{F}_{cap,2}|$) experienced by the aggregates de-encapsulating from the two drops. **(e)** Expected

17

variation of the quantities V_{agg}, h_{de}, $|\mathbf{H}|$, $|\mathbf{F}_{mag}|$, and $|\mathbf{F}_{cap}|$ with V_d and c_{MNP}. The same variations in

V_{agg} and h_{de} can be noted in the experimental results provided in parts (b) and (c).

Mechanistic explanation of the Nanoaggregate De-encapsulation:

The nanoaggregate de-encapsulation primarily occurs when the nanoaggregate (of length scale, l) breaches and crosses the drop-PDMS interface by overcoming the drop-PDMS surface-tension force (which is proportional to l) in presence of the driving magnetic force and the gravitational force (with both of these forces scaling as l^3). Under these circumstances, it becomes increasingly difficult for a particle to escape the interface with decreasing length scale, which is also the reason why the problem of de-encapsulation and magnetic extraction is an alluring one. Consequently, we do not observe individual MNPs diffusing across the drop-PDMS interface (for this case, the capillary force on the individual MNPs is strong enough to balance the magnetic plus gravitational pull); rather, the interface is breached (thereby leading to the complete de-encapsulation) by the *MNP aggregate* (MNPs aggregated as a clump) having a vertically elongated shape [see Fig. 3(d)]. A sequential representation of the de-encapsulation process (*via* both schematic diagrams and experimental snapshots) is presented in **Figures 4(a-d)**.

The mechanism that we proposed is based on the assumption that the particles have aggregated sufficiently, such that the aggregate acts as a single body that is big enough to overcome the surface-tension force in presence of the driving magnetic and gravitational pull. This systematic aggregation is possibly enhanced by the magnetic chaining [42-44], which has been known to enrich the phase-separation of magnetic particles and also provide a certain rigidity to the aggregate. The de-encapsulation is associated with the formation of a neck (at the location of the drop from which the aggregate de-encapsulates) that is the precursor of the de-encapsulation step [see **Figures 4(c,d)**]. We predict the necking distance as the distance from the substrate, where the maximum achievable upward force on the aggregate is balanced by the downward forces. We call this the necking distance because beyond this point, the drop is bound to de-encapsulate as the

19

upward forces only decrease in magnitude whereas downward forces increase exponentially. We argue that since the time difference between drop necking and de-encapsulating is fairly negligible, necking distance must be a good representative (substitute) for de-encapsulation distance (h_{de}). Below, we provide a quantitative description of these different forces acting on the aggregate.

The maximum surface-tension force that pulls the drop (aggregate) upward will occur when the water-PDMS surface is pulling the aggregate entirely upwards at the maximum circumference of the aggregate. The time instance where this happens is marked by water-PDMS interface getting parallel to the vertical plane as shown in **Figure 4(e)**. We do the force balance (in z direction) as described below.

Force acting on the aggregate due to gravity is given by:

$$F_{grav} = -\rho_{agg}V_{agg}g. \tag{1}$$

Force acting on the aggregate due to buoyancy is given by:

$$F_{buoy} = \rho_{PDMS}V_{agg}g. \tag{2}$$

Force due to surface tension:

$$F_{ST} = \gamma L_c = \gamma . 2\pi r_{agg}\cos\theta, \tag{3}$$

where γ water-PDMS surface tension, r_{agg} is the radius of the characteristic length $2\pi r_{agg}$, and $\cos\theta$ is the cosine of the angle between the tangent of the aggregate boundary and the deformed drop boundary (here $\cos\theta = 1$) at the point of de-encapsulation,

Force corrections due to Laplace pressure of the drop are accounted for in the surface tension force calculation (R_d is the radius of the bulk drop) as given by:

20

$$F_{ST} = \gamma . 2\pi r_{agg} \left(1 - \frac{r_{agg}}{R_d}\right). \tag{4}$$

The magnetic force acting on the aggregate due to the imposed non-linear magnetic field is given by:

$$F_{mag} = -\mu_0 {\mu_{MNP}}^2 \chi_{MNP} V_{agg} \frac{1}{2} \frac{\partial}{\partial z}(H^2). \tag{5}$$

Thus, the force balance on the aggregate about to be extracted can be written as:

$$F_{grav} + F_{buoy} + F_{ST} + F_{mag} = 0. \tag{6}$$

Here, since the magnetic field strength H varies with position, F_{mag} is also a function of the z coordinate. Hence, inverting eq. (6) will give us h_{de}. We have two input variables from the experimental setup: drop volume V_d and MNPs concentration C_{MNP}. Furthermore, R_d, r_{agg} and V_{agg} can be expressed as:

$$R_d = \left(\frac{3V_d}{4\pi}\right)^{1/3}, \tag{7}$$

$$V_{agg} = V_d \lambda C_{MNP}/\rho_{MNP}, \tag{8}$$

$$r_{agg} = \left(\frac{3V_{agg}}{4\pi\varepsilon}\right)^{1/3}, \tag{9}$$

where, λ is the extraction fraction of MNPs from the drop and ε is the elongation of the aggregate.

Unfortunately, determining γ and μ_{MNP} is beyond the scope of this paper. To account for the missing constants in our model, we select two experimental points, $(V_d, C_{MNP})_1$ and $(V_d, C_{MNP})_2$ and its corresponding de-encapsulation distance h_{de1} and h_{de2} at random and solve eq. (6) to get γ and μ_{MNP}. We see that the final curves for h_{de} vs V_d is not affected significantly by the choice

21

of the random points. We show our predicted trends in **Figures 4(f-h)**, and it can be seen that the

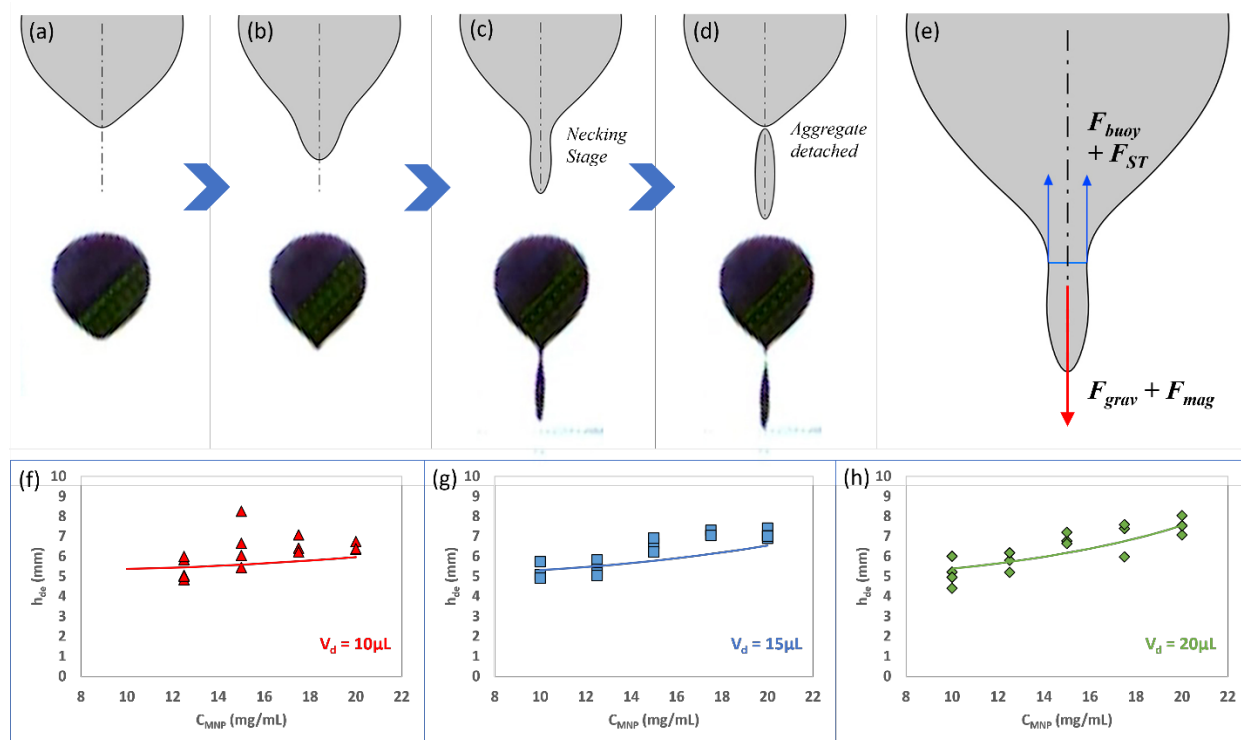predictions from our theoretical model aptly satisfy the experimental findings.

Figure 4. (a-d) Schematic (top panel) and actual experimental snapshots (bottom panel) showing a sequential progression of the MNLD to de-encapsulation. The experimental results are for the same conditions represented in Fig. 1(c). **(a)** shows the onset of aggregation of MNPs. **(b)** shows a significant aggregation and hence deformation of the drop. **(c)** is the instance when we see a first occurrence of necking. We define this as the necking stage, and the corresponding height of the necking zone as the necking height. **(d)** shows the final detachment of the nanoaggregate. **(e)** Schematic showing the force balance where we balance the buoyancy, F_{buoy} and maximum surface tension, F_{ST} on the nanoaggregate with the gravitational, F_{grav} and magnetic, F_{mag} forces on the nanoaggregate. **(f-h)** Comparison of the experimental findings of the h_{de}-vs-C_{MNP} variation with the corresponding theoretical predictions corresponding **(f)** V_d = 10 μL, **(g)** V_d = 15 μL, and **(h)** V_d = 20 μL. The comparison confirms a decent match between the experimental and the theoretical predictions.

23

Conclusion:

In this paper we have laid down the first example where, counterintuitively, the magnetic nanoparticles, dispersed in liquid drops (in a high-viscous PDMS medium) aggregates and de-encapsulates out of the drop under the action of magnetic force overcoming the strong resisting drop-PDMS capillary forces. Given the severity of such capillary forces, such complete de-encapsulation of particles from the interior of a drop is a very rare event, and to the best of our knowledge, this is the first study that shows that. We identify the distance where this de-encapsulation happens, the corresponding time it takes, and the volume of detached aggregate across a broad range of concentration of magnetic nanoparticles and volume of the drop. Higher concentration and higher volume are shown to promote the drop de-encapsulation against a fixed external magnetic field. To explain the trends, we identified the relevant dynamic forces acting on the drop-PDMS-nanoparticles system and gave a set of equations to predict the de-encapsulation distance outside the studied range of parameters. Finally, we anticipate that this study will form the basis of a technology that will enable an on-demand deposition of nanoparticles (at desired locations and in desired amount) that will serve a host of applications ranging from targeted drug delivery to additive manufacturing.

References

1. Thiévenaz, V., & Sauret, A. (2022). The onset of heterogeneity in the pinch-off of suspension drops. *Pro. Natl. Acad. Sci. USA*, *119*(13). doi: 10.1073/pnas.2120893119

2. Park, B.S., Jung, K.I., Lee, S.J., Lee, K.Y., & Jung, H.W. (2018). Effect of particle shape on drying dynamics in suspension drops using multi-speckle diffusing wave spectroscopy. *Colloid Polym. Sci.*, *296*(5), 971–979. doi: 10.1007/s00396-018-4315-x

3. Jørgensen, L., Forterre, Y., & Lhuissier, H. (2020). Deformation upon impact of a concentrated suspension drop. *J. Fluid Mech.*, *896*. doi: 10.1017/jfm.2020.394

4. Grishaev, V., Iorio, C.S., Dubois, F., & Amirfazli, A. (2017). Imapct of particle-laden drops: particle distribution on the substrate. *J. Colloid Interface Sci., 490*, 108-118. doi: 10.1016/j.jcis.2016.11.038

5. Harbottle, D. Bueno, P., Isaksson, R., & Kretzschmar, I. (2011). Coalescence of particle-laden drops with a planar oil-water interface. *J. Colloid Interface Sci., 362*, 235-241. doi: 10.1016/j.jcis.2011.05.077

6. Shao, X., Duan, F., Hou, Y., & Zhong, X. (2020). Role of surfactant in controlling the deposition patter of a particle-laden droplet: Fundamentals and strategies. *Adv. Colloid Interface Sci., 275*, 102049. doi: 10.1016/j.cis.2019.102049

7. Parthasarathy, D., Thampi, S. P., Ravindran, P., & Basavaraj, M. G. (2021). Further Insights into Patterns from Drying Particle Laden Sessile Drops. *Langmuir*, *37*(14), 4395–4402. doi: 10.1021/acs.langmuir.1c00512

8. Skarżyński, K., Krzemiński, J., Jakubowska, M., & Słoma, M. (2021). Highly conductive electronics circuits from aerosol jet printed silver inks. *Sci. Rep.*, *11*(1). https://doi.org/10.1038/s41598-021-97312-5

9. Gu, Y., Park, D., Gonya, S., Jendrisak, J., Das, S., & Hines, D.R. (2019). *Addit. Manuf., 30*, 100843. doi: 10.1016/j.addma.2019.100843

10. Yan, K., Li, J., Pan, L., & Shi, Y. (2020). Inkjet printing for flexible and wearable electronics. *APL Materials*, *8*(12), 120705. doi: 10.1063/5.0031669

11. Lemarchand, J., Bridonneau, N., Battaglini, N., Carn, F., Giorgio Mattana, Piro, B., Samia Zrig, & Noël, V. (2022). Challenges, Prospects, and Emerging Applications of Inkjet-Printed Electronics: A Chemist's Point of View. *Angewandte Chemie*, *61*(20). doi: 10.1002/anie.202200166

12. Eremeeva, E., Ekaterina Sergeeva, Valeriia Neterebskaia, Morozova, S., Kolchanov, D., Morozov, M., Chernyshov, I., Milichko, V., & Vinogradov, A. (2020). Printing of Colorful Cellulose Nanocrystalline Patterns Visible in Linearly Polarized Light. *ACS Appl. Mater. Interfaces*, *12*(40), 45145–45154. doi: 10.1021/acsami.0c11846

13. Ahmed Simon, A., Badamchi, B., Subbaraman, H., Sakaguchi, Y., Jones, L., Kunold, H., J. van Rooyen, I., & Mitkova, M. (2021). Introduction of Chalcogenide Glasses to Additive Manufacturing: Nanoparticle Ink Formulation, Inkjet Printing, and Phase Change Devices Fabrication. *Sci. Rep.*, *11*(1). doi: 10.1038/s41598-021-93515-y

14. Wang, C-S., Friedlander, S.K., & Madler, L. Nanoparticle aerosol science and technology: an overview. (2005). *China Particuology, 3*(5), 243-254. doi: 10.1016/S1672-2515(07)60196-1

15. Haghani, A., Johnson, R., Safi, N., Zhang, H., Thorwald, M., Mousavi, A., Woodward, N. C., Shirmohammadi, F., Coussa, V., Wise, J. P., Forman, H. J., Sioutas, C., Allayee, H., Morgan, T. E., & Finch, C. E. (2020). Toxicity of urban air pollution particulate matter in developing and adult mouse brain: Comparison of total and filter-eluted

nanoparticles. *Environment International*, *136*, 105510. doi:
10.1016/j.envint.2020.105510

16. Ha, N., Seo, E., Kim, S., & Lee, S. J. (2021). Adsorption of nanoparticles suspended in a drop on a leaf surface of Perilla frutescens and their infiltration through stomatal pathway. *Sci. Rep.*, *11*(1). doi: 10.1038/s41598-021-91073-x

17. Li, Y., Khuu, N., Prince, E., Moien Alizadehgiashi, Galati, E., Lavrentovich, O. D., & Kumacheva, E. (2019). Nanoparticle-laden droplets of liquid crystals: Interactive morphogenesis and dynamic assembly. *Sci. Adv.*, *5*(7). doi: 10.1126/sciadv.aav1035

18. Melton, C. N., Riahinasab, S. T., Keshavarz, A., Stokes, B. J., & Hirst, L. S. (2018). Phase Transition-Driven Nanoparticle Assembly in Liquid Crystal Droplets. *Nanomaterials*, *8*(3), 146–146. doi: 10.3390/nano8030146

19. Alves, V. M., Nakamatsu, S., Oliveira, E. A., Zappone, B., & Richetti, P. (2009). Anisotropic Reversible Aggregation of Latex Nanoparticles Suspended in a Lyotropic Nematic Liquid Crystal: Effect of Gradients of Biaxial Order. *Langmuir*, *25*(19), 11849–11856. doi: 10.1021/la901520r

20. Zargartalebi, H., Hejazi, S. H., & Sanati-Nezhad, A. (2022). Self-assembly of highly ordered micro- and nanoparticle deposits. *Nat. Commun.*, *13*(1). doi: 10.1038/s41467-022-30660-6

21. Yunker, P. J., Still, T., Lohr, M. A., & Yodh, A. G. (2011). Suppression of the coffee-ring effect by shape-dependent capillary interactions. *Nature*, *476*(7360), 308–311. doi: 10.1038/nature10344

22. Nguyen, T. A. H., Hampton, M. A., & Nguyen, A. V. (2013). Evaporation of Nanoparticle Droplets on Smooth Hydrophobic Surfaces: The Inner Coffee Ring Deposits. *J Phy. Chem. C*, *117*(9), 4707–4716. doi: 10.1021/jp3126939

23. Rahimi, M., Roberts, T. F., Armas-Pérez, J. C., Wang, X., Bukusoglu, E., Abbott, N. L., & de Pablo, J. J. (2015). Nanoparticle self-assembly at the interface of liquid crystal droplets. *Proc. Nat. Acad. Sci.*, *112*(17), 5297–5302. doi: 10.1073/pnas.1422785112

24. A. Khan, M., & F. Haase, M. (2021). Stabilizing liquid drops in nonequilibrium shapes by the interfacial crosslinking of nanoparticles. *Soft Matter*, *17*(8), 2034–2041. doi: 10.1039/D0SM02120B

25. Li, X., Zhang, Y., Li, M., Zhao, Y., Zhang, L., & Huang, C. (2020). Convex-Meniscus-Assisted Self-Assembly at the Air/Water Interface to Prepare a Wafer-Scale Colloidal Monolayer Without Overlap. *Langmuir*, *37*(1), 249–256. doi: 10.1021/acs.langmuir.0c02851

26. Ye, Z., Li, C., Chen, Q., Xu, Y., & Bell, S. E. J. (2021). Self-assembly of colloidal nanoparticles into 2D arrays at water–oil interfaces: rational construction of stable SERS substrates with accessible enhancing surfaces and tailored plasmonic response. *Nanoscale*, *13*(12), 5937–5953. doi: 10.1039/D0NR08803J

27. Park, M., Kang, S., Nam, C., Karnati Narasimha, Won Bo Lee, & Park, S.-J. (2022). Magnetic Field-Induced Self-Assembly of Conjugated Block Copolymers and Nanoparticles at the Air–Water Interface. *ACS Appl. Mater. Interfaces*, *14*(6), 8266–8273. doi: 10.1021/acsami.1c22535

28. Chen, W., Cheng, C.-A., & Zink, J. I. (2019). Spatial, Temporal, and Dose Control of Drug Delivery using Noninvasive Magnetic Stimulation. *ACS Nano, 13*(2), 1292-1308. doi: 10.1021/acsnano.8b06655

29. Rodzinski, A., Guduru, R., Liang, P., Hadjikhani, A., Stewart, T., Stimphil, E., Runowicz, C., Cote, R., Altman, N., Datar, R., & Khizroev, S. (2016). Targeted and controlled anticancer drug delivery and release with magnetoelectric nanoparticles. *Sci. Rep.*, *6*(1). doi: 10.1038/srep20867

30. Bassetto, M., Ajoy, D., Poulhes, F., Obringer, C., Walter, A., Messadeq, N., Sadeghi, A., Puranen, J., Ruponen, M., Kettunen, M., Toropainen, E., Urtti, A., Dollfus, H., Zelphati, O., & Marion, V. (2021). Magnetically Assisted Drug Delivery of Topical Eye Drops Maintains Retinal Function In Vivo in Mice. *Pharmaceutics*, *13*(10), 1650. doi: 10.3390/pharmaceutics13101650

31. Ulbrich, K., Holá, K., Šubr, V., Bakandritsos, A., Tuček, J., & Zbořil, R. (2016). Targeted Drug Delivery with Polymers and Magnetic Nanoparticles: Covalent and Noncovalent Approaches, Release Control, and Clinical Studies. *Chem. Reviews*, *116*(9), 5338–5431. doi: 10.1021/acs.chemrev.5b00589

32. Lee, S., Ahn, J.-H., Choi, H., Seo, J.M., Cho, D., & Koo, K. (2015, August 25-29). Natural magnetic nanoparticle containing droplet for smart drug delivery and heat treatment. *37th Annual International Conference of the IEEE Engineering in Medicine and Biology Society.*

33. Li, Z., Yang, F., & Yin, Y. (2020). Smart Materials by Nanoscale Magnetic Assembly. *Adv. Funct. Mater.*, *30*(2), 1903467–1903467. doi: 10.1002/adfm.201903467

29

34. Deng, K., Luo, Z., Tan, L., & Quan, Z. (2020). Self-assembly of anisotropic nanoparticles into functional superstructures. *Chem. Soc. Rev.*, *49*(16), 6002–6038. doi: 10.1039/D0CS00541J

35. Lee, M. S., Yee, D. W., Ye, M., & Macfarlane, R. J. (2022). Nanoparticle Assembly as a Materials Development Tool. *J Am. Chem. Soc.*, *144*(8), 3330–3346. doi: 10.1021/jacs.1c12335

36. Li, X., Dong, Z.-Q., Yu, P., Wang, L.-P., Niu, X.-D., Yamaguchi, H., & Li, D.-C. (2021). Effect of self-assembly on fluorescence in magnetic multiphase flows and its application on the novel detection for COVID-19. *Phys. Fluids*, *33*(4), 042004. doi: 10.1063/5.0048123

37. Li, J., Zhang, J., Guo, Z., Jiang, H., Zhang, H., & Wang, X. (2020). Self-Assembly Fabrication of Honeycomb-like Magnetic-Fluorescent Fe_3O_4-QDs Nanocomposites for Bimodal Imaging. *Langmuir*, *36*(48), 14471–14477. doi: 10.1021/acs.langmuir.0c00077

38. Lindemann, M.C., Luttke, T., Nottrodt, N., Schmitz-Rode, T., & Slabu, I. (2021). FEM based simulation of magnetic drug targeting in a multibranched vessel model. *Comput. Methods Programs Biomed., 210*, 106354. doi: 10.1016/j.cmpb.2021.106354

39. Mackolil, J., & Mahanthesh, B. Inclined magnetic field and nanoparticle aggregation effects on thermal Marangoni convection in nanoliquid: A sensitivity analysis. *Chi. J. Phys., 69*, 24-37. doi: 10.1016/j.cjph.2020.11.006

40. Shi, S., & Russell, T. P. (2018). Nanoparticle Assembly at Liquid–Liquid Interfaces: From the Nanoscale to Mesoscale. *Adv. Mater. 30*(44), 1800714. doi: 10.1002/adma.201800714

41. Mendoza, A.J., Guzman, E., Martinez-Pedrero, F., Ritaco, H., Rubio, R.G., Ortega, F., Starov, V.M., and Miller, R. (2014). Particle laden fluid interfaces: Dynamics and

interfacial rheology. *Adv. Colloid Interface Sci. 206*, 303-319. doi: 10.1016/j.cis.2013.10.010

42. Karvelas, E.G., Lampropoulos, N.K., Benos, L.T., Karakasidis, T., & Sarris, I.E. On the magnetic aggregation of Fe_3O_4 nanoparticles. *Comput. Methods Programs Biomed., 198*, 105778. doi: 10.1016/j.cmpb.2020.105778

43. Dominik, C., Nubold, H. Magnetic Aggregation: Dynamics and Numerical Modeling. *Icarus, 157*(1), 173-186. doi: 10.1006/icar.2002.6813

44. Shimada, K., Miyazaki, T., Shibayama, A., and Fujita, T. (2002). Extraction of magnetic particle clusters self-assembled by a magnetic field. Smart Mater. Struct. 12, 297-303. doi: 10.108/0964-1726/12/2/318

Supporting Information

Magnetic Nanoparticle Aggregation and Complete De-Encapsulation of Such Aggregates from a Liquid Drop Interior

Swarup Kumar Subudhi, Ghansham Ranjendrasingh Chandel, Vishal Sankar Sivasankar, and Siddhartha Das*

Department of Mechanical Engineering, University of Maryland, College Park, MD 20742

*Email: sidd@umd.edu

S1. Materials and Methods
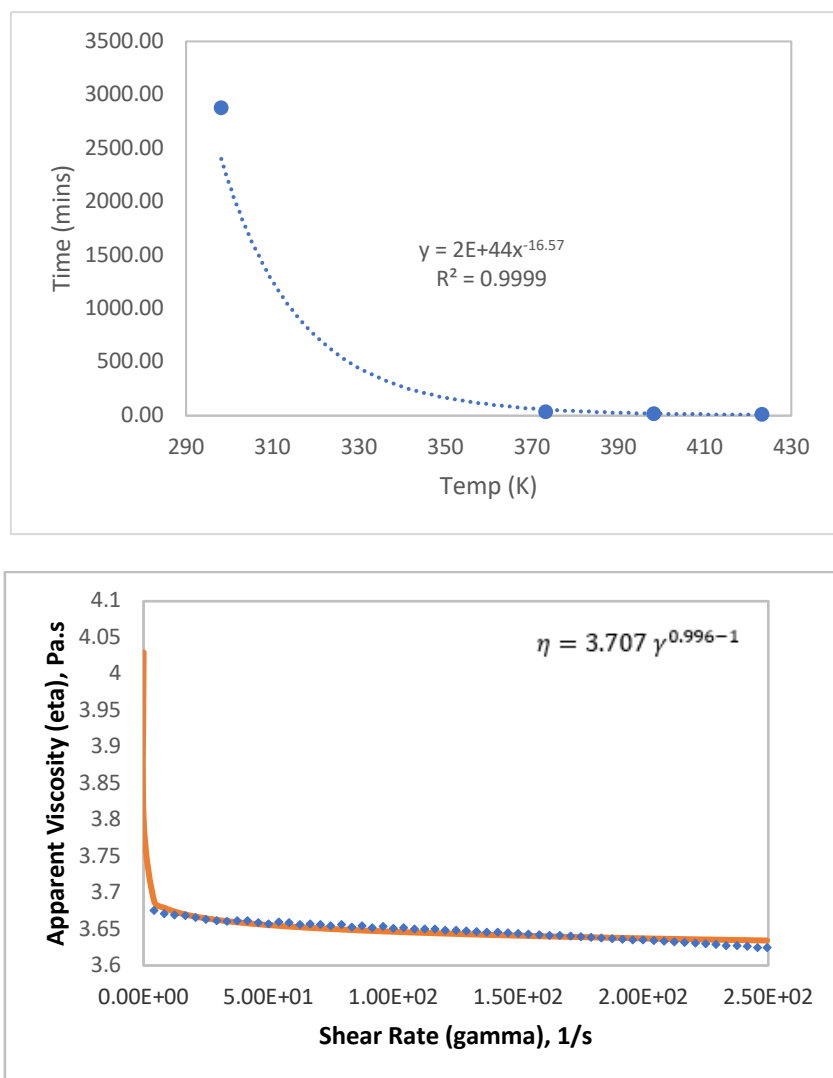
1. *Characterization of PDMS:*

Figure S1. (a) Curing curve for Sylgard-184 (PDMS A+B) at room temperature ($T_{amb} = 25°C$).

The curing curve was created by extrapolating the curing data points provided in the Sylgard-184

Silicone Elastomer Technical Datasheet [https://www.dow.com/documents/11/11-3184-sylgard-

184-elastomer.pdf?iframe=true]; (b) Rheology of used crosslinked PDMS medium, extrapolated

33

using the power law model: $\eta = m\dot{\gamma}^{n-1}$, where η is the apparent viscosity, $\dot{\gamma}$ is the shear rate, and m and n are constants.

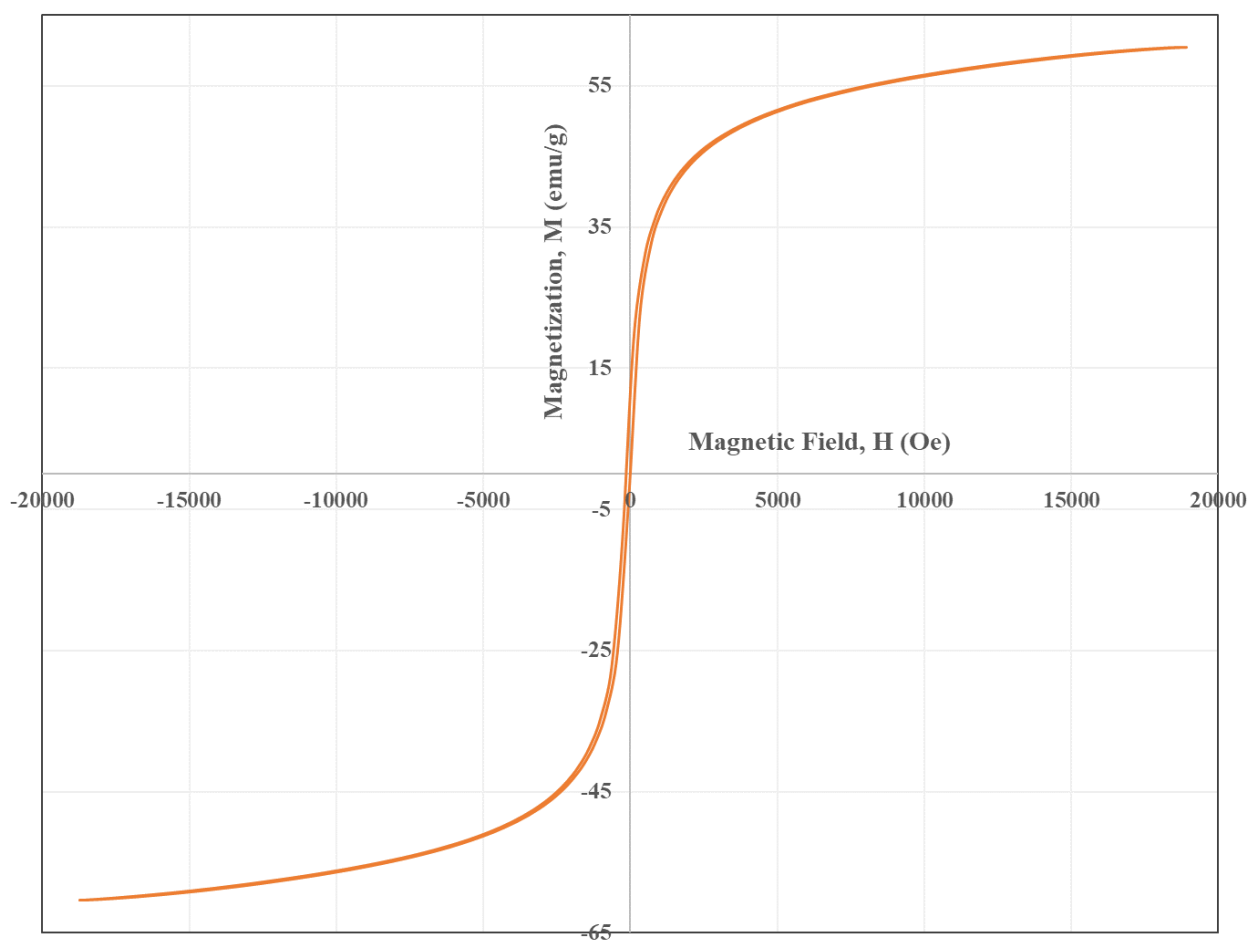## 2. Characterization of PVP-coated Fe₃O₄ NPs:

Figure S2. Magnetization curve of PVP-coated Fe₃O₄ NPs (as measured in the Lakeshore Model 7460 VSM equipment).
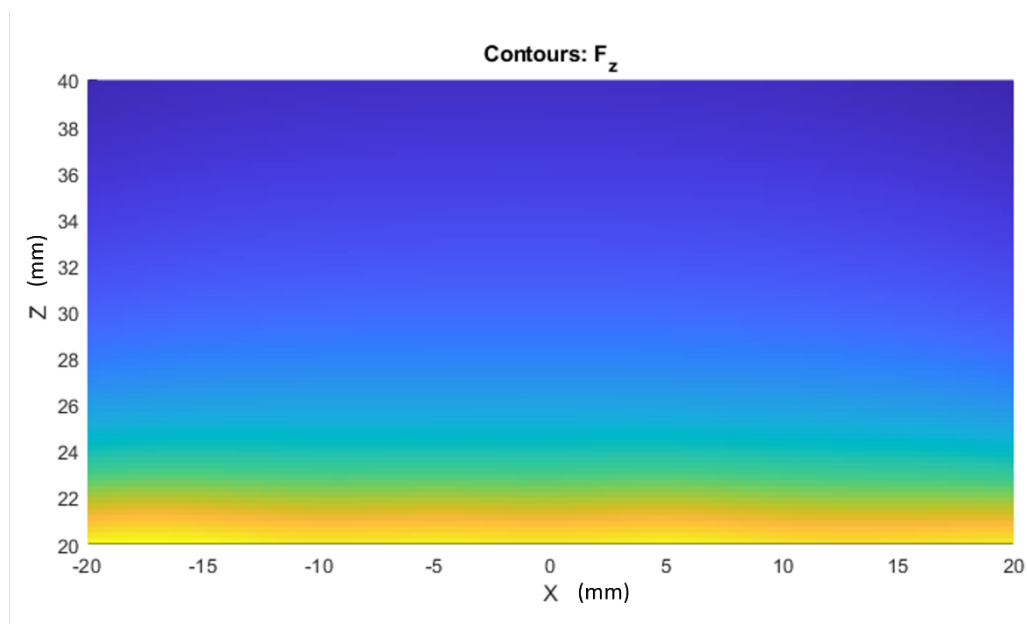
S2. Characterization of Magnetic Field:

Figure S3. Contours of the magnetic field strength in the X-Z plane (where z = 20 denotes the top of the magnet stack in the experimental setup, and x = 0 denotes the mid-plane of the bar magnets). The contours are plotted from z = 20mm to 40mm, which is the working range for the setup.

35

S3. Aggregate Volume Data Extraction

The images captured by both the cameras were brought to the same scale for further processing. A MATLAB code was used to measure the volume of the aggregate extracted from the 2D images using an elliptical interpolation method as shown in Figure S3. Initially, the portion of the image containing the extracted aggregate was cropped and the aggregate image area was isolated by using thresholding functions available in Image Processing toolbox of MATLAB. The resultant working images from both X-Z and Y-Z viewing planes were converted to segmented images for further processing as shown in the figure. The segmentation step size was taken as $\Delta h = 1$ pixel. The center line was calculated as the midpoint of the mean pixel lengths of each vertical pixel step, and the corresponding elliptical axes a_{i1} and a_{i2} (for X-Z); and b_{i1} and b_{i2} (for Y-Z) were computed. The volume of the extracted aggregate was calculated as:

$$V_{agg} = \sum_{i=1}^{N} \frac{\pi}{2} \bar{a}_{i1} \bar{b}_{i1} \Delta h + \sum_{i=1}^{N} \frac{\pi}{2} \bar{a}_{i2} \bar{b}_{i2} \Delta h$$
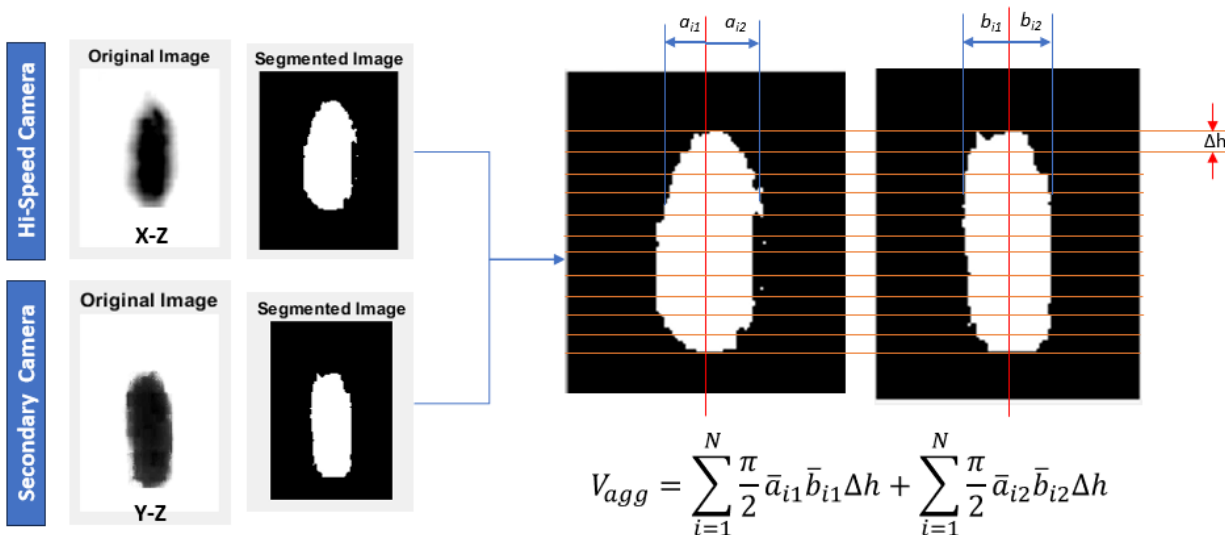
where N is the total number of pixel steps.

Figure S4. Schematic of the extracted aggregate volume (V_{agg}) computation algorithm.